et al., the existence of a plasmon line was not reported, even for small values of the momentum transfer. This, we assume, is due to their very large experimental width which is of the order of 22 eV and therefore would overlap the plasmon band. In our experiments the experimental width is of the order of 11 eV.

In conclusion, we observe that in Fig. 2 the peak of the plasmon line is well separated from TDS and Compton lines which overlap. In Fig. 3 the spectra for $\phi = 17°$, $20°$, and $25°$ allow the separate observation of the TDS and the plasmon peak. The Compton band is observed as a weak bump.

The observed line is due to the bulk plasmon and no attempt has been made to detect higher-order plasmons. However, in the case of $\phi = 6.5°$ it might be possible to attribute the bump at the far left to a second-order plasmon.

ACKNOWLEDGMENT

The author would like to thank Professor F. Alexopoulos for his encouragement and suggestions in carrying out this work.

*Work supported in part by the National Hellenic Research Foundation.

[1]G. Priftis, K. Alexopoulos, and A. Theodossiou, Phys. Letters 27A, 577 (1968).

[2]G. Priftis, Phys. Rev. B 2, 54 (1970).

[3]A. Tanokura, N. Hitota, and T. Suzuki, J. Phys. Soc. Japan 22, 515 (1969).

[4]D. Bohm and D. Pines, Phys. Rev. 92, 609 (1953).

[5]D. Pines and D. Bohm, Phys. Rev. 85, 338 (1952).

[6]C. J. Powell, Proc. Phys. Soc. (London) 76, 593 (1960).

[7]P. Nozières and D. Pines, Phys. Rev. 113, 1254 (1959).

[8]D. Bohm, *The Many-Body Problem* (Dunod, Paris, 1959).

[9]A. J. Glick and R. A. Ferrell, Ann. Phys. (N. Y.) 11, 359 (1960).

[10]N. Swanson, J. Opt. Soc. Am. 54, 1130 (1964).

[11]D. Pines, *Elementary Excitations in Solids* (Benjamin, New York, 1964).

[12]J. Ziman, *Principles of the Theory of Solids* (Cambridge U. P., Cambridge, England, 1964).

[13]V. Krisham and R. H. Ritchie (private communication).

[14]D. F. DuBois, Ann. Phys. (N. Y.) 7, 174 (1959); 8, 24 (1959).

[15]B. W. Ninham *et al.*, Phys. Rev. 145, 209 (1966).

[16]M. Hasegawa and M. Watabe, J. Phys. Soc. Japan 27, 1393 (1969).

[17]W. Schülke, U. Berg, and O. Brummer, Phys. Status Solidi 35, 227 (1969).

[18]Y. Ohmura and N. Matsudaira, J. Phys. Soc. Japan 19, 1355 (1964).

PHYSICAL REVIEW B VOLUME 3, NUMBER 3 1 FEBRUARY 1971

Channeling of Positrons

J. U. Andersen* and W. M. Augustyniak
Bell Telephone Laboratories, Murray Hill, New Jersey 07974

and

E. Uggerhøj
Institute of Physics, University of Aarhus, 8000 *Aarhus C, Denmark*

(Received 7 July 1970)

Axial and planar channeling in thin single-crystalline gold foils has been investigated by wide-angle scattering of monoenergetic positrons. The beam was obtained by accelerating the positrons emitted from a Co^{58} source in a 1-MeV Van de Graaff. The results are in good agreement with corresponding measurements for protons. For the planar case, classical calculations are compared to calculations based on the dynamical theory of diffraction. The results are very similar except for the "wiggles" due to wave interference, which appear in the quantum-mechanical calculation. These, however, are difficult to resolve experimentally.

INTRODUCTION

The aim of this experiment is to shed some light on the question of applicability of classical channeling theory to the directional effects observed for emission of electrons and positrons from a single crystal. In Uggerhøj's measurements[1,2] of the angular distribution of electrons and positrons emitted from Cu^{64} implanted in copper single crystals, a quantitative comparison with theory or with heavy-particle channeling was difficult because of the radiation damage incurred during the implantation of the radioactive ions into the crystal. The results for positrons, however, were consistent

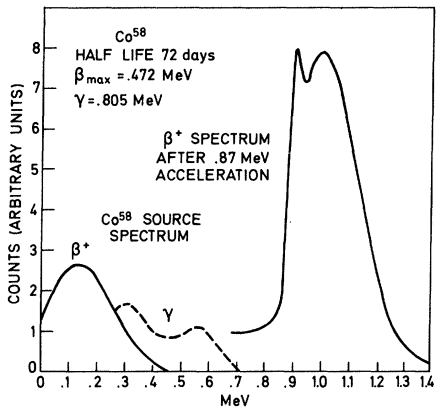

FIG. 1. Source spectrum, before and after acceleration.

with a classical interpretation.

Because of reversibility (or reciprocity), the same information can be obtained in an experiment where the yield of some close-encounter process is measured as a function of incidence direction of an external beam on a single crystal. In such an experimental configuration, the radiation damage of the crystal is avoided. Practically all the quantitative information on heavy-particle channeling has been obtained in this way. This paper reports such an investigation of positron channeling. Parallel investigations for electrons will be published separately (see also Ref. 3).

For positrons, experiments with an external beam present special difficulties. The problem of obtaining a positron beam is discussed below. The low-beam intensity necessitates the use of a reaction with large cross section. For this reason, forward Rutherford scattering in a thin single crystal was detected. The use of a thin crystal also has the advantage of defining the reaction depth. In a thick target, this is difficult to do because of the small energy-loss rate for relativistic positrons.

For the first studies of channeling of a positron beam Behnisch *et al.* used a thick crystal.[4] The yield of characteristic x rays showed a strong dip for positron incidence parallel to a major axis. As stated by the authors, this result is difficult to understand since the x rays originate from an estimated mean depth of ~ 50 μm. At such large depths one would expect most of the positrons to be dechanneled due to multiple scattering.

Note added in proof: Recently Walker *et al.*[5] have observed channeling dips in both scattering yield and Bremsstrahlung yield for very high energy positrons in rather thin silicon crystals.

POSITRON BEAM

The main experimental difficulty is to obtain a monenergetic well-collimated positron beam. This was solved by mounting a ~ 50-mCi Co^{58} source in the terminal of a 1-MeV electron Van de Graaff. The Co^{58} was embedded in a 0.6-mm resin bead and mounted on a gold backing. Some of the source characteristics and the measured positron spectrum are shown in Fig. 1. It is seen that the half-life is convenient and that, furthermore, both the β and the γ energies are fairly low. Only 16% of the decays, however, involve β^+ emission.

The spectra in Fig. 1 illustrate the advantages obtained by the acceleration. These spectra are obtained with a silicon solid-state detector and correspond approximately to the same counting time and the same distance from the source. The β spectrum before acceleration has a maximum at ~ 130 keV. After 0.87-MeV acceleration, the spectrum looks somewhat different. The peak at 130 keV now corresponds to a peak at ~ 1 MeV, but another very sharp peak has appeared at the lower side of the spectrum. This may be explained by the focusing due to the acceleration. Consider a positron emitted from the source at an angle θ_0 to the axis of the Van de Graaff, with momentum p_0. The transverse momentum is given by $p_\perp \simeq \theta p$ and is not changed by the acceleration, $\theta p = \theta_0 p_0$. Thus, the angle θ is inversely proportional to the momentum p, and the intensity of positrons within a fixed solid angle is proportional to p^2. In terms of the kinetic energy of the positrons, the intensity is proportional to $(E_{\rm kin} + 2m_0c^2)E_{\rm kin}$. The enhancement factor f is then given by

$$f = \frac{(E^0_{\rm kin} + eV + 2m_0c^2)(E^0_{\rm kin} + eV)}{(E^0_{\rm kin} + 2m_0c^2)E^0_{\rm kin}} , \qquad (1)$$

where $E^0_{\rm kin}$ is the kinetic energy before acceleration and V is the acceleration potential. For small initial energies, obviously f can become very large, thus giving rise to the sharp peak at the lower side of the spectrum. The calculated value of the enhancement factor f is ~ 5 for $E_{\rm kin} = 130$ keV and $V = 0.87$ MV.

Thus, the first advantage of the acceleration is a gain in total intensity within a fixed solid angle. The second advantage is a reduction of the relative energy spread by almost a factor of 8. For both reasons, a low $\beta_{\rm max}$ is desirable. Finally, one can discriminate against the γ background after acceleration. This background is mainly due to Compton scattering of the 0.8-MeV γ radiation and the 0.5-MeV annihilation radiation from the source. The relatively low energy of the γ radiation is an advantage here.

EXPERIMENTAL ARRANGEMENT

Figure 2 shows schematically the experimental arrangement. The Co^{58} source is mounted in the terminal of a 1-MeV electron Van de Graaff with reversed polarity. The beam is focused by a fo-

cusing magnet and collimated by two collimators to within 0.14°–0.3°. The beam intensity was 5–60 particles per sec, depending on collimation and time (source decay). This is considerably lower than might be expected from source strength and solid angle. The main reduction is due to absorption in the resin bead.

The crystal is mounted in a goniometer allowing two perpendicular tilts. An annular solid-state silicon detector counts positrons scattered to approximately 4°–10°, and a forward detector counts the positrons transmitted through the central hole of the annular detector. The multiple scattering angle is small compared to the acceptance angle for the annular detector, so that single scattering is detected. [Measurements[6] of the multiple scattering of 1-MeV electrons in a 1200-Å thick polycrystalline gold foil give a mean scattering number of ~3 and a full width at half-maximum (FWHM) of ~1.2° for the scattered part of the angular distribution.] The crystal used was a 1200-Å-thick gold single crystal.[7] The thickness was determined by an energy-loss measurement using 1-MeV helium ions.

EXPERIMENTAL PROCEDURE

The experimental procedure was similar to the standard procedure for heavy-particle channeling measurements. The orientation of the crystal was first determined using the planar dips. In these initial scans, counting times of ~2 min per point were sufficient. For some of the detailed scans with good collimation, counting times of ~2 h per point were necessary.

The normal (random) yield was sometimes difficult to determine from an axial scan. It was then obtained from a scan at some angle to the string.

Most of the γ background was eliminated by energy discrimination. For incidence parallel to a string, however, the contribution to the yield was not negligible. During each scan, the contribution was measured several times. This background has been subtracted from the experimental curves.

RESULTS

A. Strings

Figure 3 shows the dip along the closest packed axis in gold, the ⟨110⟩ axis. The dip is very strong,

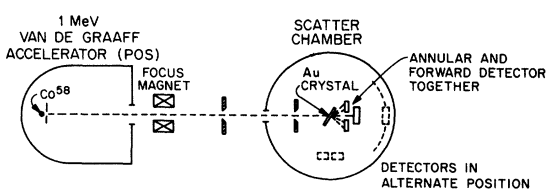

FIG. 2. Experimental arrangement.

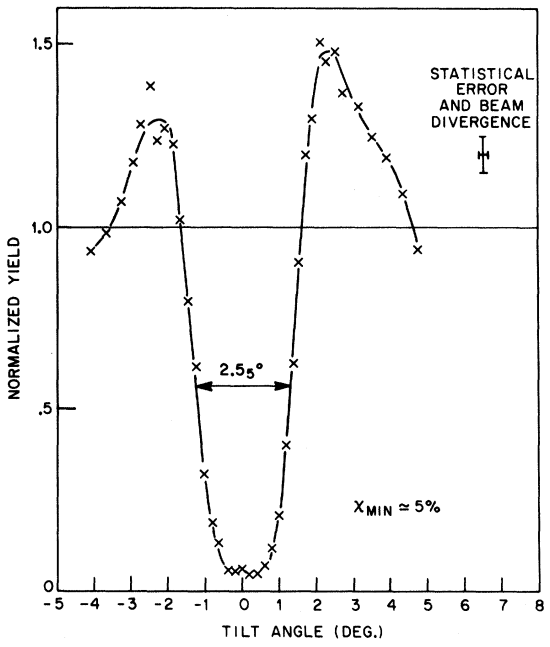

FIG. 3. Measured dip along the closest packed direction in gold, the ⟨110⟩ axis, $d = 2.8$ Å.

about a factor of 20. The background correction applied in this case was only ~1%. The width of the dip is somewhat smaller than that calculated from classical channeling theory. The characteristic angle ψ_1 for a string with atomic spacing d is given by

$$\psi_1 = (2Z_1Z_2e^2/\tfrac{1}{2}pvd)^{1/2} \qquad (2)$$

for relativistic particles.[8] In this case $\psi_1 \simeq 2°$, corresponding to an expected full width of ~4°. The rather large thermal vibrations in gold should lead to a width lower by a factor of ~0.8,[9] assuming that the rms vibrational amplitude ρ, measured perpendicular to the string, is 0.12 Å. The observed width is lower than this estimate by about 20%. Since discrepancies of this magnitude are not uncommon for heavy-particle channeling (see, e.g., Ref. 10), a more decisive test is a comparison with the experimentally determined dip for proton scattering in gold.

Such a comparison is shown in Fig. 4. The proton dip was measured for 1-MeV protons, using backscattering from part of the same gold sample, mounted on a silver backing. Backscattering from the silver was eliminated by energy discrimination of the backscattered protons. Since for relativistic particles it is half the product of the momentum and the velocity (i.e., $\frac{1}{2}pv$) that enters in Eq. (2) rather than the kinetic energy, 1-MeV positrons should be compared to 670-keV protons. For heavy particles, it is well established that the

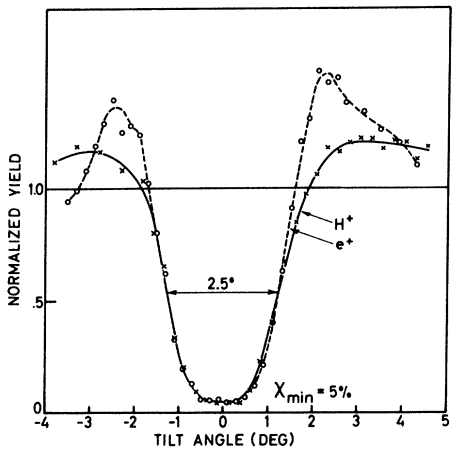

Fig. 4. Comparison of positron and proton dips along the ⟨110⟩ axis. The abscissa scale for the proton dip has been scaled from 1 to 0.67 MeV (see text).

width is proportional to $E^{-1/2}$ for not too low energies, hence the abscissa scale for the proton curve has been multiplied by a factor of $(1.0/0.67)^{1/2}$ before comparison. The two curves are independently normalized to random yield as described above.

The resulting agreement is very striking. The minimum yields and the widths are in almost perfect agreement. The shoulders, on the other hand, are quite different. This, however, is not surprising since the shoulders are very sensitive to the azimuthal angle of the string scan.[11] [Another possible explanation may be mentioned. At angles of incidence $\psi \lesssim \psi_1$, there is enhanced scattering to directions corresponding to conservation of the angle relative to the string (i.e., conservation of transverse energy). The minimum acceptance angle of the detector is in fact about twice the angle of incidence corresponding to the shoulder region.] It can be concluded that for this case possible quantal corrections to the classical picture are quite small.

The string dip has been measured for several other less prominent axes. Figure 5 shows the dip along the ⟨111⟩ axis. This dip is only a factor of ~7 and considerably narrower than the ⟨110⟩ dip. Table I summarizes the measured widths of the three most prominent axes. According to Eq. (2), the width should be inversely proportional to the square root of the spacing d of the atoms in the string. This prediction is quite well fulfilled.

TABLE I. Measured widths of the three most prominent axes.

Axis	$2\psi_{1/2}$	$\psi_{1/2}/\psi_{1/2}(\langle 110\rangle)$	$(d_{\langle 110\rangle}/d)^{1/2}$
⟨110⟩	2.55°	1	1
⟨112⟩	1.90°	0.75	0.76
⟨111⟩	1.50°	0.59	0.64

B. Planes

Measurements. Planar dips would be expected to exhibit more structure due to interference phenomena than string dips. In Fig. 6, a measured {111} dip is compared with the result of a 13-beam calculation. Clearly, the fine structure due to wave interference is not resolved. The beam intensity was too low to allow significant improvement of the collimation. A similar scan and calculation are shown in Fig. 7 for the {110} plane. In this case there are indications of "wiggles," but the statistical accuracy is not very good. This observation was, however, supported by several other {110} scans showing wiggles with the right periodicity.

Again, the most decisive comparison is one with an identical measurement for protons. Table II shows the results of such a comparison. The minimum yields and the widths agree within the experimental accuracy. The proton measurement was again performed at 1 MeV, and before comparison the width was scaled to 670 keV.

Calculations. In the planar case, both a classical and a dynamical diffraction calculation are reasonably easy to do. Figure 8 shows a comparison of the resulting {111} dips.

The 13-beam calculation is based on the dynamical theory of electron diffraction. Similar calculations have been published by several authors (see, e.g. Ref. 12). The present calculations were based on the formulation in Ref. 13 (Chap. 12) of multiple-beam theory. For a given angle of incidence, the wave function in the crystal is calculated as a sum

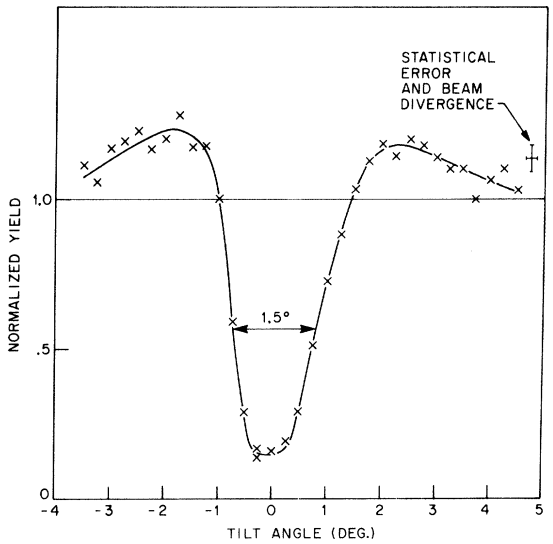

FIG. 5. Measured dip along the ⟨111⟩ direction $d = 7.0$ Å.

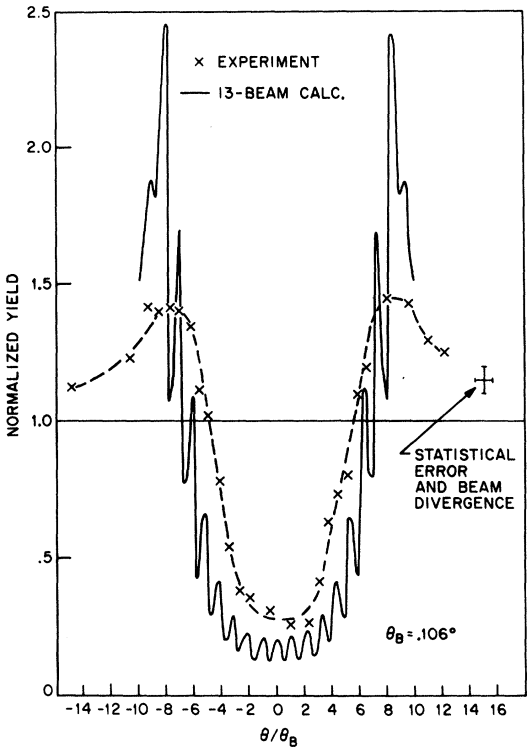

FIG. 6. Comparison of measured dip for a {111} plane with a 13-beam calculation. The planar spacing is d_p = 2.35 Å. θ_B denotes the Bragg angle; $\theta_B = \lambda/2d_p$.

of Bloch waves with excitation amplitudes determined by matching the wave function of the surface to an incoming plane wave. The scattering yield is assumed to be proportional to the intensity of the wave function at the position of the atomic planes. Interference terms between different Bloch waves are neglected.[14] For this comparison with the classical calculations, the Fourier components of the potential were calculated from Lindhard's standard potential.[15] Debye-Waller factors were omitted corresponding to the use of a static potential in the classical calculations. The yield was calculated in the region $0 < \theta < 10\theta_B$, taking into account Bragg reflections of order − 4 to 8. The full curve was then obtained from symmetry.

The classical curves were computed according to the formulas in Ref. 9. (There is a misprint in formula (16) in Ref. 9. The factor $\{E\psi_1^2 + Y(y)]/E\psi_1^2\}^{1/2}$ should be deleted.) For both classical curves, the motion of the particles is described as the motion in an average (static) planar potential. But whereas the full-drawn curve describes the probability of hitting static atoms in the plane, the dashed curve describes the probability of hitting atoms vibrating around a mean position in the plane. Since the dynamical calculation does not include this smearing of the atomic positions, it should in principle be compared with the full-drawn curve. The difference, however, is seen to disappear when thermal vibrations are taken into account. This should, of course, be done in a similar way in the 13-beam calculation, but would probably not change the result very much since the positrons are not localized much better than to within $\sim \rho$ in such a calculation (i.e., the wave function does not vary much over distances smaller than ρ).

Phase-space estimates. Some information on the validity of a classical description may be gained from estimates of the number of quantum states contained in the potential minimum. Semiclassically, this number is given by the available phase space divided by the proper power of Planck's constant h. In the string case, the effective potential barrier for the transverse motion is of the order of $\frac{1}{2}pv\psi_1^2$, corresponding to a critical angle ψ_1. The accessible area in the transverse plane is $\sim (Nd)^{-1}$, where N is the density of atoms and d is the atomic spacing in the string. For the number of quantum states, we then obtain

$$n \simeq \pi(p\psi_1)^2/h^2Nd \quad . \tag{3}$$

TABLE II. {111} planar dips.

Particle	Width	χ_{min}
H^+	1.2°	26%
e^+	1.1°	28%

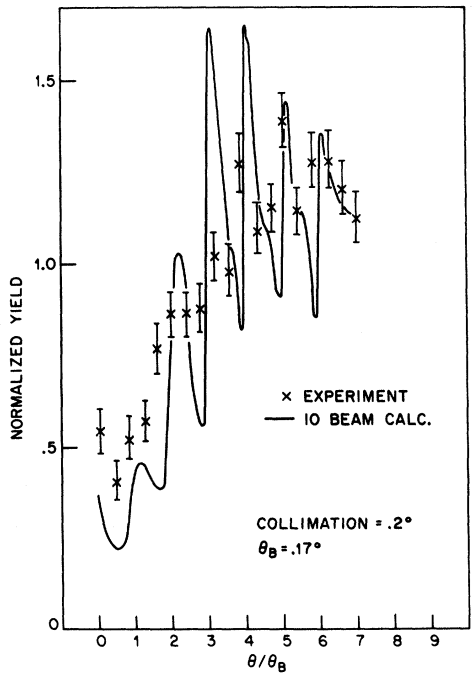

FIG. 7. Measured and calculated {110} planar dip d_p = 1.44 Å. θ_B denotes the Bragg angle; $\theta_B = \lambda/2d_p$.

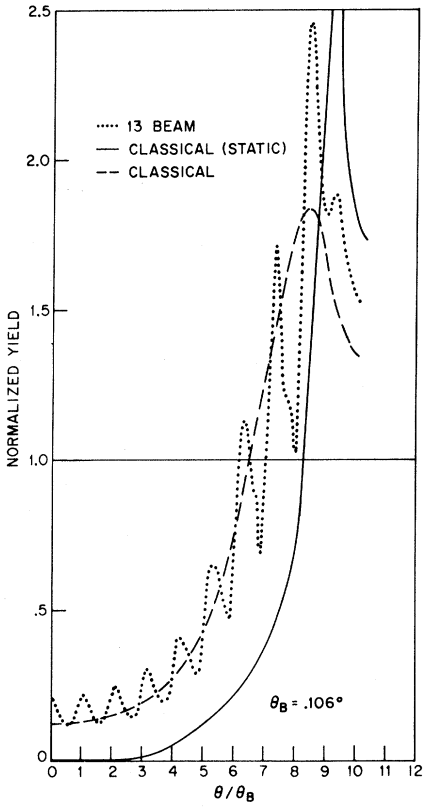

FIG. 8. Comparison of classical calculations with a 13-beam calculation for the {111} planar dip. θ_B denotes the Bragg angle; $\theta_B = \lambda/2d_p$.

Inserting Eq. (2), we get

$$n \simeq Z_2 \gamma/\pi N d^2 a_0 \ , \tag{4}$$

where γm_0 is the relativistic mass and a_0 is the Bohr radius, $a_0 = \hbar^2/m_0 e^2$. For the present cases, $n \gtrsim 10^2$.

For planes, a simple estimate is

$$n \simeq 2p\psi_c d_p/h \ . \tag{5}$$

The critical angle for planar channeling, ψ_c, may be calculated from the transverse planar potential. It is smaller than the critical angle ψ_1 belonging to strings by roughly a factor of $2Z_2^{1/6}$.[15]

Introducing the Bragg angle $\theta_B = \lambda/2d_p$, we get

$$n \simeq \psi_c/\theta_B \ . \tag{6}$$

For the calculation in Fig. 6, this number is $n \simeq 8$.

Tunneling. When the number of quantum states is large, a classical description may be appropriate. The transverse energy (or momentum) is then quantized into bits small compared to the potential barrier. Channeling into classically forbidden regions should then be considered. In Ref. 8, the following cursory estimates of the penetration factor are given for nonrelativistic positrons of small transverse energy,

$$T \sim \exp[-6(Z_2^{1/3} a_0/d)^{1/2}] \tag{7}$$

for strings, and

$$T \sim \exp[-15(N d_p a_0^2)^{1/2}] \tag{8}$$

for a plane. For relativistic positrons, the exponent should be multiplied by $\gamma^{1/2}$. In the present case, where $\gamma = 3$, these formulas lead to $T \sim 10^{-4}$ and $T \sim 0.5 \times 10^{-2}$ for the ⟨110⟩ axis and the {111} plane, respectively. While this would indicate that tunneling in the axial case is not very important, the significance of the estimate is less clear in the planar case. The classical distribution in transverse energy for incidence parallel to a plane is not very strongly peaked at $E_\perp \sim 0$. One might qualitatively attribute the difference in Fig. 8 between the classical and the many-beam calculations to tunneling. These calculations, however, also indicate that the importance of tunneling is strongly reduced when thermal vibrations are taken into account.

CONCLUSIONS

Axial and planar channeling of 1-MeV positrons in gold may essentially be described by classical mechanics. This conclusion is mainly based on a comparison with proton channeling. For planar channeling, a comparison between classical and dynamical diffraction calculations also shows essential agreement. These results are consistent with phase-space estimates for the string and planar potentials, which indicate that the number of quantum states involved is large, especially in the axial case. Also effects of tunneling should be rather small. The collimation and statistical accuracy achieved in this experiment were marginal for the observation of interference "wiggles" in planar channeling.

ACKNOWLEDGMENTS

We wish to thank our colleagues, especially Dr. W. L. Brown, Dr. L. C. Feldman, and Dr. J. Lindhard for encouragement and many stimulating discussions. Thanks are also due to F. Frandsen for performing the proton measurements and, in particular, to P. Ambrosius-Olesen for providing the high-quality thin gold crystals. One of us (E. U.) also wishes to thank Bell Telephone Laboratories for financing a stay at Murray Hill during the month when most of the measurements were performed.

*Present address: Institute of Physics, University of Aarhus, 8000 Aarhus C, Denmark.

[1] E. Uggerhøj, Phys. Letters 22, 382 (1966).
[2] E. Uggerhøj and J.U. Andersen, Can. J. Phys. 46,

543 (1968).
[3]E. Uggerhøj and F. Frandsen, Phys. Rev. B 2, 582 (1970).
[4]R. Behnisch, F. Bell, and R. Sizmann, Phys. Status Solidi 33, 375 (1969).
[5]R. L. Walker, B. L. Berman, R. C. Der, T. M. Kavanagh, and J. Khan, Phys. Rev. Letters 25, 5 (1970).
[6]F. Frandsen and E. Uggerhøj (unpublished).
[7]W. M. Gibson, J. B. Rasmussen, P. Ambrosius-Olesen, and C. J. Andreen, Can. J. Phys. 46 551 (1968); L. Chadderton and M. Andersen, Thin Films 1, 229 (1969).
[8]P. Lervig, J. Lindhard, and V. Nielsen, Nucl. Phys. A96, 481 (1967).
[9]J. U. Andersen, Kgl. Danske Videnskab. Selskab, Mat.-Fys. Medd. 36, No. 7 (1967).
[10]S. T. Picraux, J. A. Davies, L. Eriksson, N.G.E. Johansson, and J. W. Mayer, Phys. Rev. 180, 873 (1969).
[11]J. U. Andersen and E. Uggerhøj, Can. J. Phys. 46, 517 (1968).
[12]R. E. DeWames and W. F. Hall, Acta Cryst. A24, 206 (1968).
[13]P. B. Hirsch, A. Howie, R. B. Nicholson, D. W. Pashley, and M. J. Whelan, *Electron Microscopy of Thin Crystal* (Butterworths, London, 1965).
[14]C. R. Hall, Proc. Roy. Soc. (London) A295, 140 (1966).
[15]J. Lindhard, Kgl. Danske Videnskab. Selskab, Mat.-Fys. Medd. 34, No. 14 (1965).

PHYSICAL REVIEW B VOLUME 3, NUMBER 3 1 FEBRUARY 1971

Covalency Effects on the 3*d*-Charge-Density Distribution in Solid Ferrous Compounds

Y. Hazony
Department of Chemical Engineering, Princeton University, Princeton, New Jersey 08540
(Received 18 June 1970)

A phenomenological description of the 3*d*-charge-density distribution in solids, based on Mössbauer hyperfine interaction data, studies of crystal structures, EPR, neutron scattering and optical spectroscopy, has been developed for divalent iron ions in solids. From this work, it appears that one can obtain an internally consistent picture of the 3*d*-charge-density distribution in solids by allowing for large, but distinctly different, modifications of the radial $3d(e_g)$ and $3d(t_{2g})$ electronic wave functions. These modifications vary continuously with covalency on going from the completely ionic to the completely covalent ferrous compounds. They account for the large changes (in order of magnitude) in the mean 3*d* charge (or spin) densities, indicated by the experimental data. These results cannot be explained by theoretical models of bonding based on crystal field and molecular-orbital theories, using *free-ion* wave functions. The present model emphasizes the importance of the radial modifications of the 3*d* wave functions, thus supporting the point of view that, in self-consistent-field-type theoretical computations, the radial wave functions should be described by variational rather than fixed parameters.

I. INTRODUCTION

A major difficulty in understanding bonding in the solid state is the lack of an adequate set of electronic wave functions. The use of "free-ion" wave functions is justified only by the lack of anything better. An important step toward understanding the effects of covalency on 3*d* electronic wave functions has been made by Alperin who measured the neutron-scattering form factor for Ni^{2+} in solids.[1] His results show a significant contraction of the $3d(e)$-spin-density distribution, with respect to the predictions from free-ion calculations, which is in contrast with the apparent expansion observed for Mn^{2+} ion in solids by Hastings, Elliott, and Corliss[2]; he suggests that the discrepancy is due to the outstanding difference in the spin configurations of the two ions, e.g., e_g^2 vs $t_{2g}^3\ e_g^2$ unpaired spins.

Recently, Freeman and Ellis have reported the results of fully variational unrestricted Hartree-Fock calculations for $(MnF_6)^{4-}$ clusters.[3] These authors obtain results which resolve the above paradox. While the spin-density distribution of the two unpaired e_g electrons is contracted and that of the three unpaired t_{2g} electrons is expanded, the net effect is that of an expansion in comparison with the free-ion Mn^{2+}.[3]

These results support our phenomenological analysis of the Mössbauer isomeric shift (IS) and quadrupole splitting (QS) for the ferrous halides[4,5] and series of related compounds.[6,7] This analysis shows that a predominant effect of covalency in the high-spin octahedral ferrous compounds is the radial expansion of the $3d(t_{2g})$ wave functions.

In the present work we analyze the Mössbauer hyperfine interactions of two series of octahedral, high-spin, and ionic, as well as intermediate ferrous compounds in terms of the radial distribution